Multiphysics modelling of magnetic Curie point materials: Application to thermal self-regulation during induction heating

Hakim Oueslati, Guillaume Wasselynck, Didier Trichet, Simon Morville

Journal of Magnetism and Magnetic Materials 631 (2025) 173496

Contents lists available at ScienceDirect

Journal of Magnetism and Magnetic Materials

journal homepage: www.elsevier.com/locate/jmmm

Research article

Multiphysics modelling of magnetic Curie point materials: Application to thermal self-regulation during induction heating

Hakim Oueslati [a,b,*], Guillaume Wasselynck [a], Didier Trichet [a], Simon Morville [b]

[a] Nantes Université, Institut de Recherche en Énergie Électrique de Nantes Atlantique, IREENA, UR 4642, F-44600 Saint-Nazaire, France
[b] Institut de Recherche Technologique Jules Verne, 1 Mail des 20 000 lieux, Bouguenais, 44340, France

ARTICLE INFO

Keywords:
Curie temperature
Ferromagnetic alloys
Magnetothermal coupling
Thermal self-regulation

ABSTRACT

Controlled Curie point materials are considered innovative due to their property of abrupt magnetic extinction when their temperature exceeds a specific threshold. This property could be used to make them very suitable for a variety of industrial processes that require temperature self-regulation. The use of these materials in magnetic induction heating may allow the power transfer to be greatly reduced at the Curie point, ensuring precise control of the heating process. However, recent developments have enabled the design of customisable materials, where the Curie threshold can be precisely adjusted during the manufacturing process in a range from ambient temperature to several hundred degrees. This tunability is commonly achieved in FeNi-based alloys, where the Curie temperature is controlled by adjusting the composition ratio of nickel and iron. Other alloying elements, such as aluminium or rare earth metals, can also be incorporated to further modify the magnetic and thermal properties. Therefore, designers need modelling tools to handle these phenomena. In this paper, a two-dimensional coupled electromagnetic and thermal model for the induction heating of magnetic materials with a low Curie point temperature is developed to validate the proof of concept.

1. Introduction

In recent years, metallurgists have developed innovative material solutions combining low Curie point alloys with aluminium or even stainless steel to achieve self-regulated induction heating, particularly for cooking utensils [1,2]. However, the concept of ferromagnetic alloys with a low Curie temperature is not new, as pioneering studies date back to the work of P. Chevenard nearly a century ago [3].

These ferromagnetic materials lose their magnetic properties when the temperature exceeds a specific threshold, corresponding to the Curie temperature. As a result, energy transfer by electromagnetic induction could be greatly reduced, opening the door to thermal self-regulation of the process without sensors. This threshold is typically around 800 °C. However, by adjusting the alloy composition, it is now possible to develop materials with a tunable Curie point, ranging from ambient temperature up to 800 °C, opening new perspectives for temperature-sensitive applications.

The temperature range opens interesting perspectives for the production of thermoplastic (preforming, forming, welding, ...) and thermoset composites (polymerisation, recycling, ...) for the aerospace industry, where precise temperature control is essential, with target temperatures often close to the degradation threshold. Although these materials have been utilised in various applications, including magnetic hyperthermia [4], thermal control of induction cooking devices [2], the design of self-regulating soldering irons [5], and the development of smart nanocomposites for uniform heating materials [6], their potential in the field of composites remains largely unexplored.

When alternating current is supplied to the coil, the transmitted power increases as a function of temperature, as seen in Fig. 1, due to the nonlinearity of ferromagnetic material properties. When the Curie temperature is reached, the material becomes paramagnetic, inducing a collapse in the magnetic permeability property. As a result, the induced power is strongly reduced, causing the temperature to fall.

The material regains its ferromagnetic property as soon as the temperature drops below the Curie point, and eddy currents increase, opening the door to open-loop thermal self-regulation of the process without the use of sensors.

The main objective of this paper is to evaluate the potential of integrating these materials in the elaboration processes of glass or carbon fibre composites through the implementation of multiphysics and multiscale finite element modelling that integrates the strong magnetothermal coupling of the phenomena associated with the crossing of the Curie point.

* Corresponding author at: Nantes Université, Institut de Recherche en Énergie Électrique de Nantes Atlantique, IREENA, UR 4642, F-44600 Saint-Nazaire, France.
E-mail address: hakim.oueslati@univ-nantes.fr (H. Oueslati).

https://doi.org/10.1016/j.jmmm.2025.173496
Received 18 April 2025; Received in revised form 6 August 2025; Accepted 8 September 2025
Available online 15 September 2025

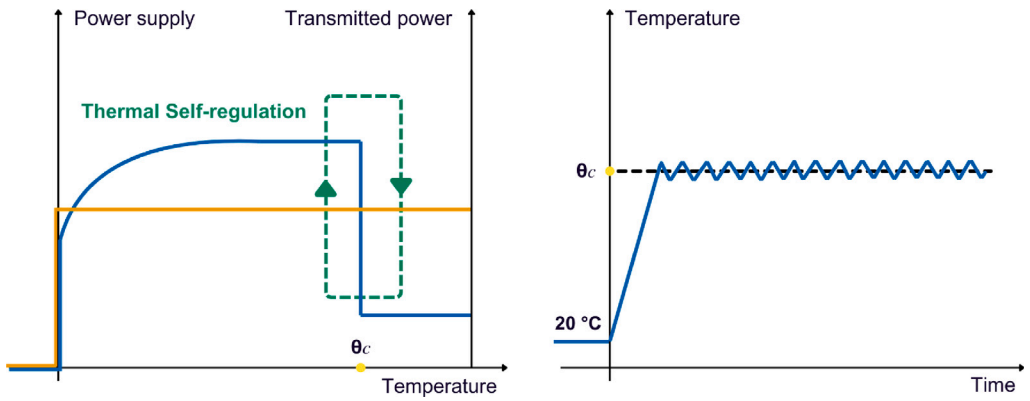

Fig. 1. Magnetothermal autoregulation.

A simulation tool must be designed to predict the behaviour of ferromagnetic materials as they approach the Curie point in electromagnetic induction heating devices. Given the heating technique employed and the types of materials processed, several challenges must be addressed, particularly the dual nonlinearity of magnetic parameters to temperature and magnetic field [7,8]. This nonlinearity results in meshing challenges, as the magnetic parameters vary significantly with the temperature near the Curie point, leading to variations in skin depth [9]. Another scientific issue is the strong magnetothermal coupling, which leads to an excessive number of unknowns and, therefore, long simulation times.

In a previous study, a one-dimensional (1D) electromagnetic and thermal model was initially developed to understand the physical phenomena behind the induction heating of Curie materials, overcome meshing difficulties, and ensure reasonable simulation times. The electromagnetic model is based on analytically solving the magnetic field equation obtained by combining Maxwell's equations. For the thermal component, the heat equation, expressed in terms of temperature T, was solved numerically using the finite difference method [10]. This coupling of electromagnetic and thermal effects enabled a detailed simulation of the temperature evolution within the material, accounting for complex interactions with the magnetic field. The analysis of thermal dynamics revealed a slope discontinuity around the Curie point, confirming thermal self-regulation and demonstrating that the induced power decreases sharply as the magnetic permeability drops abruptly at this transition [11].

Although this 1D model is highly useful for simple configurations, it remains limited in its ability to capture complex spatial phenomena, particularly in geometries where thermal and electromagnetic gradients vary significantly in multiple directions. This limitation motivates the transition to a two-dimensional (2D) model that incorporates spatial effects in both dimensions and solves the electromagnetic and thermal equations using the finite element method (FEM).

In this paper, a two-dimensional magnetothermal model is proposed to predict the behaviour of a ferromagnetic material heated by electromagnetic stimulation. The experimental magnetisation data are then adjusted to predict the magnetic permeability values at high magnetic fields suitable for induction heating. This involves finding an analytical model that can describe the set of experimental measurements with the least numerical error. The magnetothermal coupling is illustrated by an algorithm integrating the magnetic nonlinearity of this material as well as its thermal nonlinearity. Numerical linearisation and temporal approximation methods are used to ensure the modelling of the physical phenomena involved in the induction heating of a Curie point material. Simulation results such as induced power and temperature curves according to time are presented, and an analysis is provided to confirm whether the main objective of thermal self-regulation without the use of sensors can be achieved.

Table 1
Composition of Phytherm260®.

Element	Ni	Cr	Fe
Typical percentage (%)	50	9	Bal

2. Adjustment of magnetic data

The material under study is the ferromagnetic alloy Phytherm260® (Aperam Alloys), part of the Fe–Ni–Cr austenitic family containing 5% Ni with varying chromium content, allowing the Curie temperature T_C to be adjusted between 20 °C and 450 °C. For numerical simulations, Phytherm260® with a Curie temperature of $T_C = 280$ °C was selected [12,13] (Table 1).

Below $T_C = 280$ °C, the material retains its ferromagnetic properties, characterised by a high relative magnetic permeability μ_r.

As the material approaches its Curie point, it undergoes a critical phase transition to a paramagnetic state, characterised by an abrupt decline in relative permeability μ_r towards unity (Fig. 2).

This sharp drop in μ_r leads to a significant reduction in the material's ability to concentrate magnetic flux, thereby altering the distribution of induced currents and the resulting heating patterns. These rapid and nonlinear changes in magnetic properties pose substantial challenges in accurately modelling induction heating processes, as they necessitate the use of advanced numerical techniques to account for the abrupt loss of magnetic permeability and its effects on the thermal and electromagnetic behaviour of the system.

2.1. Nonlinear behaviour and magnetic permeability

At ambient temperature, Phytherm260® exhibits high magnetic permeability ($\mu_r \approx 10^4$ before magnetic saturation), which depends on both the magnetic field H and the temperature field T, introducing a dual nonlinearity. Accurate modelling of this dual dependency is critical for simulating the material's behaviour during induction heating, where eddy currents induce spatially and temporally varying H and T.

The material's high permeability at ambient temperature enhances magnetic flux concentration, facilitating the generation of induced currents [15].

Fig. 3 presents experimental measurements of $B(H)$ curves for Phytherm260® at different temperatures. These curves illustrate the steep drop in μ_r as the temperature approaches and reaches the Curie point (T_C), beyond which the magnetic induction B becomes nearly proportional to the applied field H, tending towards $\mu_0 H$. This behaviour highlights the need for precise modelling of permeability variations, particularly near magnetic saturation.

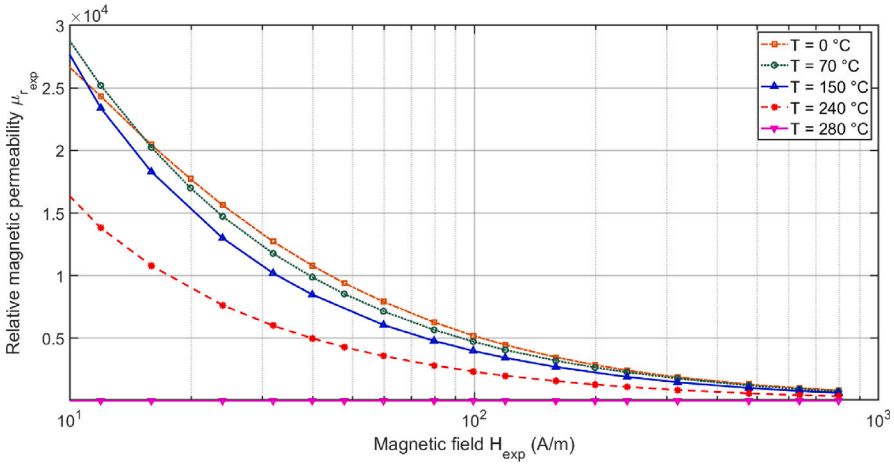

Fig. 2. Experimental $\mu_r(H)$ curves of the Phytherm260® at different temperatures [14].

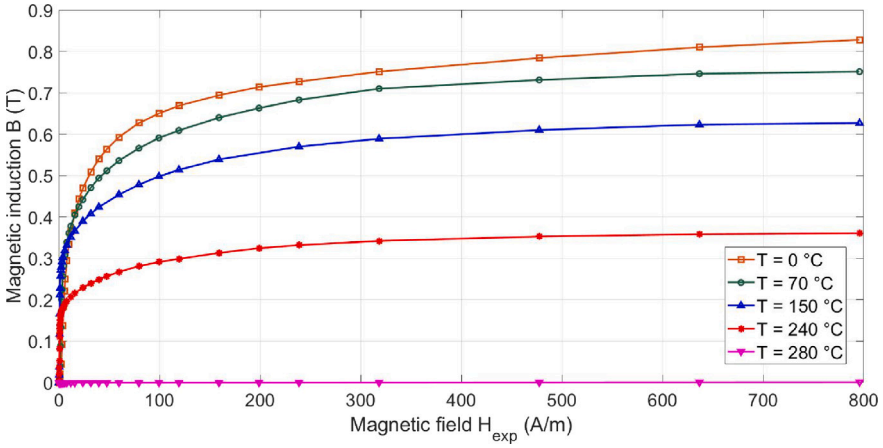

Fig. 3. Experimental $B(H)$ curves of the Phytherm260® at different temperatures [14].

2.2. Extrapolation and analytical modelling

While experimental data provide essential information, they often fail to capture the full range of μ_r behaviour at high magnetic fields or temperatures near saturation. Extrapolation techniques and analytical models, such as the Langevin model, are proposed to overcome these limitations. The Langevin model is particularly suited for describing magnetic saturation, accounting for the nonlinear response of magnetisation $B(H)$ under strong applied fields. The model is given by [16,17]:

$$B(H) = B_{\text{sat}}\left(\coth\left(\frac{H}{a}\right) - \frac{a}{H}\right) + \mu_0 H, \tag{1}$$

where B_{sat} is the saturation induction, and a is a parameter dependent on temperature and material properties. The parameters a and B_{sat} were identified through an optimisation process based on minimising the discrepancy between simulated and experimental magnetisation curves. This was achieved by iteratively adjusting a and B_{sat} using a least-squares fitting approach applied to the measured $B(H)$ response of the material (Table 2) and then interpolated over a temperature range, from −20 °C to 280 °C in steps of 1 °C [18].

μ_r^{exp} represents the experimental relative magnetic permeability measured at the highest applied magnetic field.

The interpolation of these parameters allowed the accurate modelling of $B(H)$ and μ_r over a wide range of temperatures, including regions beyond experimental measurements. Figs. 4(a) and 4(b) illustrate the temperature dependence of a and B_{sat} and the validation of the adjustment of the experimental measurements so that the value of the magnetic permeability can be predicted at higher magnetic fields.

Table 2
Identification of Langevin model parameters a and B_{sat}.

Temperature (°C)	$a(T)$	$B_{\text{sat}}(T)$	$\mu_r^{\text{exp}}(H = 800$ A/m)
$0 < T_C$	54.91	0.83	828
$70 < T_C$	19.92	0.75	751
$150 < T_C$	4.37	0.63	627
$240 < T_C$	6.54	0.36	361
$280 > T_C$	265.27	0.001	1

2.3. Magnetic permeability according to temperature and field

The evolution of relative permeability μ_r with temperature and magnetic field strength is shown in Figs. 5 and 6. At low magnetic fields, μ_r initially increases with temperature, peaking below T_C, before sharply dropping as the material transitions to a paramagnetic state. At high magnetic fields, the saturation effect dominates, causing μ_r to decrease according to the magnetic field and to approach 1 asymptotically. These trends are critical for dynamic modelling, where μ_r must be iteratively updated in response to changes in H and T.

The obtained magnetic property for Phytherm260® serves as input parameters for the coupled magnetothermal model, described in the next section.

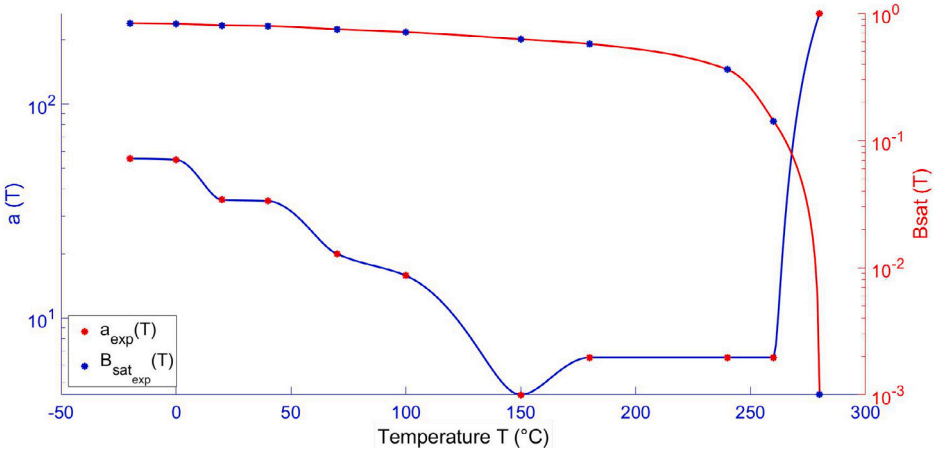

(a) Temperature dependence of Langevin model parameters a and B_{sat}.

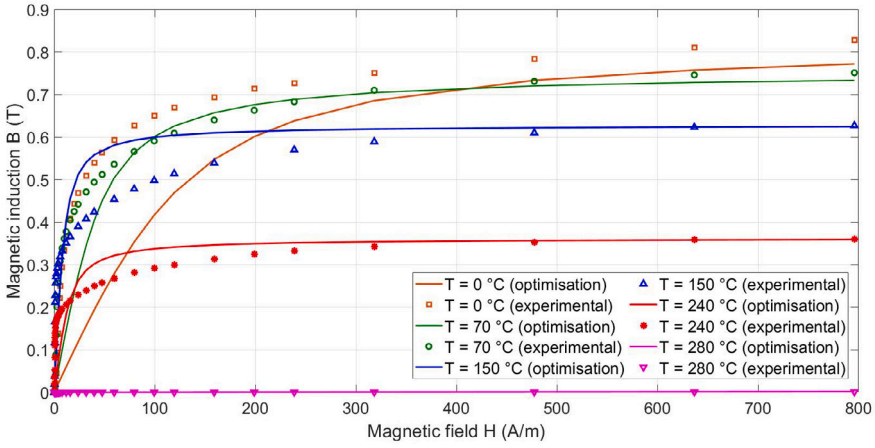

(b) Comparison between the experimental and analytically adjusted B(H) curves of the Phytherm26(at different temperatures.

Fig. 4. Adjustment of magnetic data using Langevin's analytical model.

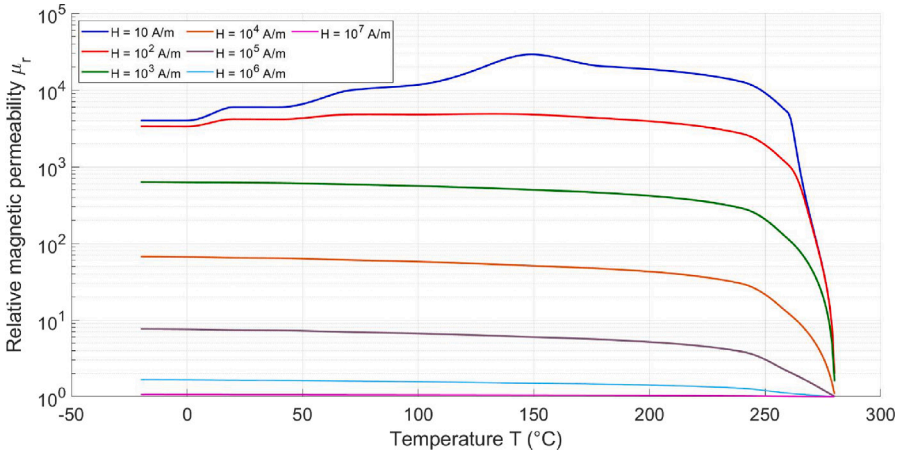

Fig. 5. Extrapolated magnetic permeability curves as a function of temperature.

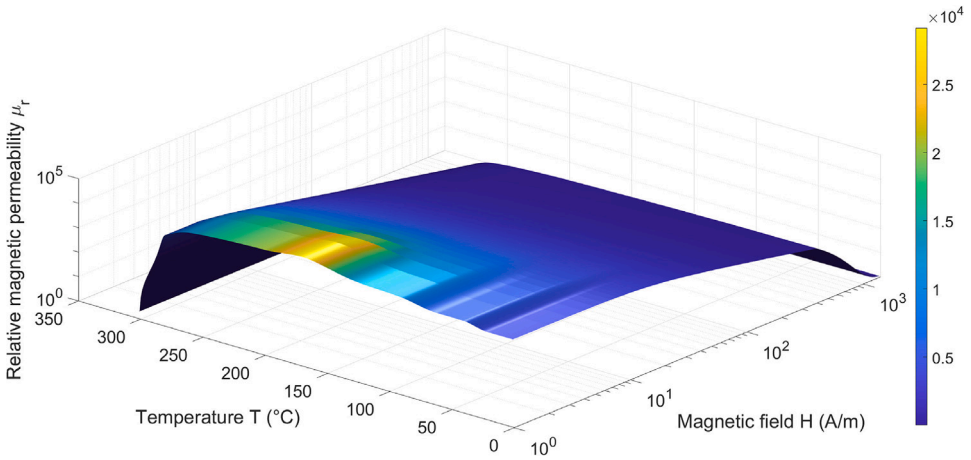

Fig. 6. Evolution of μ_r with temperature and magnetic field strength.

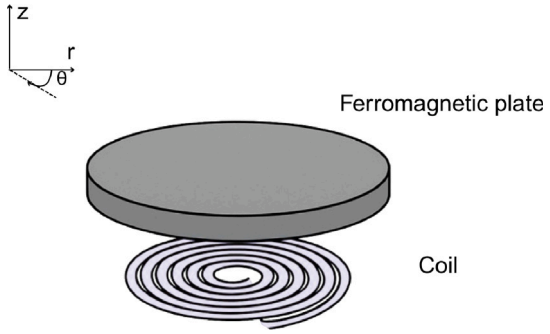

Fig. 7. Axisymmetric bidimensional geometry.

3. Development of the model

3.1. Geometry

The application considered in this study is the induction heating of a magnetic disc placed above a pancake coil powered by a current. This configuration, represented schematically in Fig. 7, which has an axis of symmetry, makes it possible to go from three-dimensional to two-dimensional, which simplifies the analysis and provides computational advantages. This setup is commonly used in various industrial applications requiring efficient and uniform heating [19].

3.2. Mesh

Once the axisymmetric geometry had been defined, it was discretised in finite element form to numerically solve for the magnetic vector potential **A** at the mesh nodes. Initially, a triangular mesh was used for this modelling. However, this approach quickly showed its limitations due to the specific constraints associated with the configuration studied and, in particular, the significant variations in magnetic permeability. In the case of ferromagnetic materials, the magnetic permeability can reach very high values, leading to a significant reduction in skin thickness, defined by the following relationship:

$$\delta = \sqrt{\frac{2}{\omega\mu\sigma}}, \tag{2}$$

where δ is the skin depth, ω is the angular frequency of the excitation current (in rad/s), μ is the magnetic permeability, and σ is the electrical conductivity.

When the permeability becomes large, the skin thickness reduces sharply (Fig. 8), concentrating the eddy currents in an extremely thin region near the surface of the ferromagnetic material. This phenomenon leads to very high gradients in the electromagnetic fields within that region.

In the context of a triangular mesh, these abrupt variations in skin thickness impose geometric constraints on the mesh elements. To capture these gradients accurately, the triangles in these regions must flatten considerably, resulting in elements with very high aspect ratios. Such a configuration can induce significant numerical errors, mainly due to the loss of accuracy in the evaluation of finite element integrals [20]. Very flattened elements degrade the quality of the mesh and amplify the errors linked to the interpolation of the fields in these critical zones [21].

Faced with these limitations, a rectangular mesh was adopted, providing a solution adapted to the specific characteristics of the problem. This choice made it possible to better manage the high gradients in areas where the magnetic permeability varies greatly while maintaining good numerical accuracy. The rectangular mesh provides better geometric regularity and limits the errors associated with excessive deformation of the elements [22,23]. It was designed to be regular in the inductor region, while a logarithmic mesh was used in the plate, air gap, and air box in the z-direction, where the logarithmic progression requires at least 3 elements in the skin depth. This approach aims to optimise resolution in the areas of interest where the field gradients are most pronounced while reducing the density of elements in the less critical regions to limit computing costs.

Fig. 9 shows the rectangular mesh produced using the GMSH software [24]. Particular attention has been paid to the fineness of the mesh in strategic regions, such as the interface between the ferromagnetic plate and the air, and in the air gap, where the gradients in the magnetic vector potential are greatest. This local refinement ensures greater accuracy in these sensitive areas while providing a gradual transition to coarser meshes in remote areas, such as the inside of the airbox. In this way, the logarithmic mesh maintains an optimal balance between numerical accuracy and computational efficiency [25].

This mesh, which contains 19 434 elements and 19 760 nodes, proved robust in solving the problem studied, significantly reducing numerical errors compared with the initial triangular mesh. It enabled the complex physical phenomena associated with electromagnetic induction heating to be modelled accurately while minimising the numerical artefacts related to geometric constraints.

3.3. Magnetic potential formulation

One establishes the vector potential formulation **A** for a magnetic problem in the magnetoquasistatic regime, assuming an axisymmetric

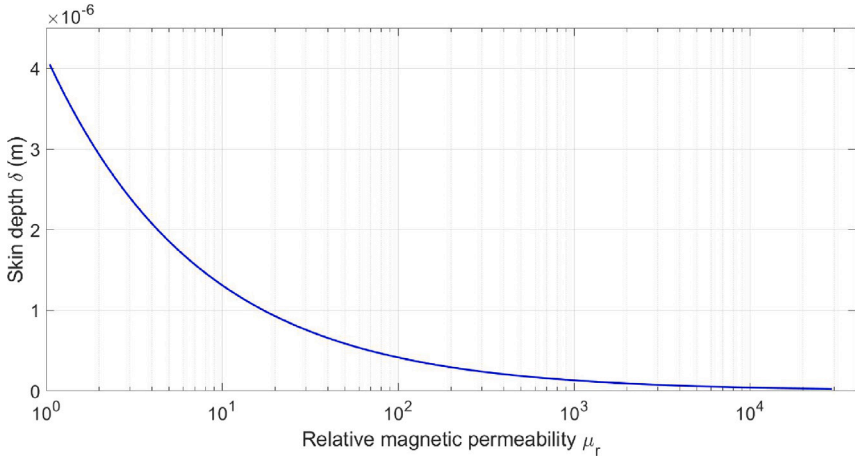

Fig. 8. Evolution of the skin depth as a function of the relative magnetic permeability.

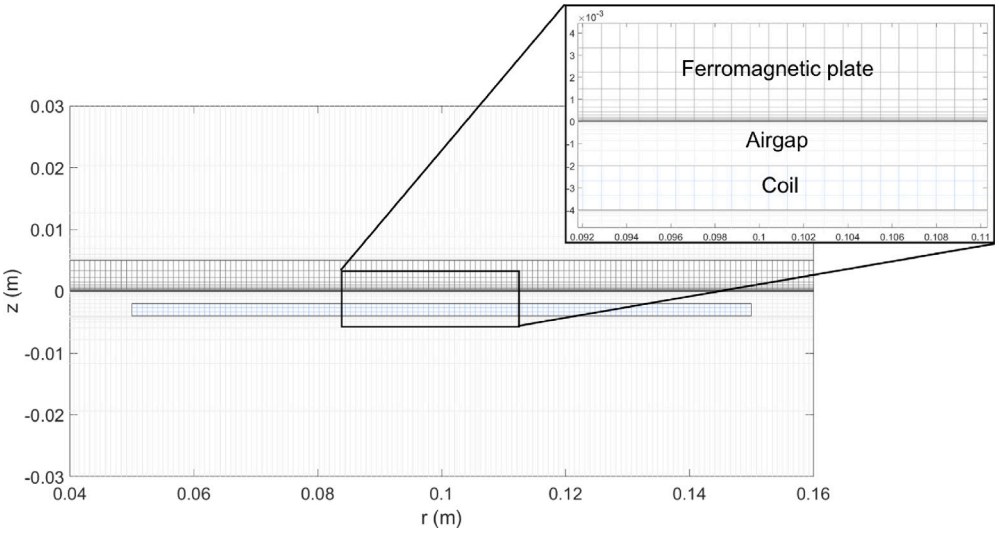

Fig. 9. Bidimensional rectangular mesh produced using GMSH [24].

configuration. This approach is commonly used in systems with cylindrical geometry, such as electrical machines, where the magnetic field exhibits rotational invariance about an axis.

For axisymmetric configurations, it is natural to adopt cylindrical coordinates (r, θ, z), where r represents the radial distance to the axis of symmetry (the z axis), θ the azimuth angle about this axis and z the coordinate along the axis. This coordinate system is particularly suitable for describing physical phenomena in cylindrical systems, such as coils and rotating structures, because it simplifies the expression of fields by taking advantage of the symmetry of the system.

In an axisymmetric problem, the physical quantities do not depend on the azimuthal angle θ. In other words, all derivatives with respect to θ are zero:

$$\frac{\partial}{\partial \theta} = 0.$$

Thus, the fields and potentials only vary as a function of the coordinates r and z. The magnetic vector potential $\mathbf{A}$ in such a context can be expressed as:

$$\mathbf{A} = A_\theta(r, z)\, \mathbf{e}_\theta, \tag{3}$$

where A_θ is the only non-zero component of $\mathbf{A}$ oriented towards $\mathbf{e}_\theta$. This reduction is a direct consequence of the invariance of the system by rotation about the axis z and means that the magnetic field generated will be contained in the plane r-z.

In coordinated cylindrical, if only A_θ is non-zero, then the magnetic field has only B_r and B_z components, given by:

$$B_r = -\frac{\partial A_\theta}{\partial z}, \quad B_z = \frac{1}{r}\frac{\partial}{\partial r}(rA_\theta). \tag{4}$$

These relations express the magnetic field induced by A_θ in the radial and axial plane.

Developing the magnetic vector formulation in cylindrical coordinates for a component A_θ only, we obtain:

$$\mathrm{div}\left(-\frac{\nu}{r}\,\mathbf{grad}\left(rA_\theta\right)\right) + \frac{\sigma}{r}\frac{\partial (rA_\theta)}{\partial t} = J_\theta^s. \tag{5}$$

Putting $A = rA_\theta$, we get:

$$\mathrm{div}\left(-\frac{\nu}{r}\,\mathbf{grad} A\right) + \frac{\sigma}{r}\frac{\partial A}{\partial t} = J_\theta^s. \tag{6}$$

To apply the finite element method and find a solution to the transient magnetic formulation, a weak formulation must be established using Green's formulae.

We apply Green's formula to the magnetic vector potential $A \in E_B^0$ and a test function A' on the first equation of the strong formulation in A and we get [26]:

$$(\nu\,\mathbf{grad}\, A, \mathbf{grad}\, A')_{L^2(D)} + \left(\sigma\frac{\partial A}{\partial t}, A'\right)_{L^2(D)} = (J_s^\theta, A')_{L^2(D)}. \tag{7}$$

The potential A is decomposed on the nodal finite elements to be injected into the formulation (7):

$$\sum_{k=1}^{n_N} A_{n_k}(t)\left(\nu\,\mathbf{grad}\,w_{n_k}(x),\mathbf{grad}\,A'(x)\right)_{L^2(D)} + \sum_{k=1}^{n_N}\frac{\partial An_k(t)}{\partial t}\left(\sigma\,w_{n_k}(x),A'(x)\right)_{L^2(D)} = \left(J_\theta^s(x),A'(x)\right)_{L^2(D)} \quad \forall\, A' \tag{8}$$

Finally, the following matrix formulation can be written [27]:

$$K\,\mathbf{A_n} + M\,\frac{\partial \mathbf{A_n}}{\partial t} = \mathbf{F} \tag{9}$$

where

$$K = \left[\left(\nu\,\mathbf{grad}\,w_{n_k}(x),\mathbf{grad}\,w_{n_l}(x)\right)_{L^2(D)}\right]_{1\le l,k\le n_N},$$
$$\mathbf{A_n} = \left[A_{n_k}(t)\right]_{1\le k\le n_N},$$
$$M = \left[\left(\sigma\,w_{n_k}(x),w_{n_l}(x)\right)_{L^2(D)}\right]_{1\le l,k\le n_N},$$
$$\mathbf{F} = \left[\left(J_s^\theta(x),w_{n_l}(x)\right)_{L^2(D)}\right]_{1\le l\le n_N}.$$

To solve this equation, numerical methods are employed. First, we discretise the time derivative using the Euler method, which gives:

$$\left(K+\frac{M}{\Delta t_{(j)}}\right)\mathbf{A}_{n_{(j+1)}} = \frac{M}{\Delta t_{(j)}}\mathbf{A}_{n_{(j)}} + \mathbf{F} \tag{10}$$

Subsequently, the nonlinear term is handled using the Newton–Raphson method, which involves linearisation. The iterative scheme for the Newton–Raphson method is expressed as:

$$(K_1^{(n+1)} + \frac{\partial \boldsymbol{K}^{(n+1)}}{\partial \mathbf{A}_{n_{(j+1)}}}\mathbf{A}^{(n)}_{n_{(j+1)}})\boldsymbol{\Delta}\mathbf{A}^{(n+1)}_{n_{(j+1)}} = \mathbf{F_1} - K_1^{(n+1)}\mathbf{A}^{(n)}_{n_{(j+1)}} \tag{11}$$

where

$$K_1 = K + \frac{1}{\Delta t_{(j)}}M,$$
$$K = \left[\left(\frac{\partial H^{(n)}}{\partial \mathbf{B}^{(n)T}}\,\mathbf{grad}\,w_{n_k},\mathbf{grad}\,w_{n_l}\right)_{L^2(D)}\right]_{1\le l,k\le n_N},$$
$$M = \left[\left(\frac{\partial \mathbf{J^i}^{(n)}}{\partial \mathbf{E}^{(n)T}}\,w_{n_k},w_{n_l}\right)_{L^2(D)}\right]_{1\le l,k\le n_N},$$
$$\boldsymbol{\Delta}\mathbf{A}^{(n+1)}_{n_{(j+1)}} = \mathbf{A}^{(n+1)}_{n_{(j+1)}} - \mathbf{A}^{(n)}_{n_{(j+1)}}.$$

3.4. Thermal formulation

A material with a thermal conductivity λ, a density ρ and a heat capacity C_p subjected to a temperature T created by a density P has a thermal behaviour defined according to the heat equation [28]:

$$\mathrm{div}\,(\lambda\,\mathbf{grad}\,T) + P = \rho\,C_p\frac{\partial T}{\partial t} \tag{12}$$

with:

- div (λ**grad** T): exchanged power density,
- P: induced power density [W m^{-3}],
- $\rho\,C_p\frac{\partial T}{\partial t}$: variation in internal energy density.

The boundary condition for heat transfer by convection at the surface is given by:

$$-\lambda\,\mathbf{grad}\,T\cdot\mathbf{n} = h(T-T_{\mathrm{amb}}) \tag{13}$$

where:

- h: heat transfer coefficient [W m^{-2} K^{-1}],
- T_{amb}: ambient temperature,
- **grad** $T\cdot\mathbf{n}$: normal temperature gradient at the surface.

The thermal formulation, containing the heat Eq. (12) and the boundary convection condition (13), is solved on the conducting domain. The time derivative $\partial_t T$ is approximated by $(T_{i+1}-T_i)/\partial T$. The heat equation is written:

$$\rho C_p\frac{T_{i+1}}{\partial T} - \mathrm{div}\,(\lambda\mathbf{grad}\,T_{i+1}) = P + \rho C_p\frac{T_i}{\partial T} \tag{14}$$

Let w_n^k be a test function for $k=1$ to N_n. Applying the weighted residual method, we obtain the following expression:

$$\int_{D_c} w_n^k\frac{\rho C_p}{\delta T}T_{i+1}\,dD - \int_{D_c} w_n^k\,\mathrm{div}(\lambda\mathbf{grad}\,T_{i+1})dD = \int_{D_c} w_n^k P\,dD + \int_{D_c} w_n^k\frac{\rho C_p}{\delta T}T_i\,dD, \quad \forall k=1,\dots,N_n. \tag{15}$$

By applying Green's identity to the second term on the left-hand side, we obtain:

$$-\int_{D_c} w_n^k\,\mathrm{div}(\lambda\mathbf{grad}\,T_{i+1})dD = \int_{D_c}\mathbf{grad}\,T_{i+1}\,\lambda\mathbf{grad}\,w_n^k dD - \int_{\Gamma_c} w_n^k\lambda\frac{\partial T_{i+1}}{\partial n}d\Gamma. \tag{16}$$

Taking into account the boundary conditions, this equation can be reformulated as follows:

$$-\int_{D_c} w_n^k\,\mathrm{div}(\lambda)\mathbf{grad}T_{i+1}\,dD = \int_{D_c}\mathbf{grad}T_{i+1}\,\lambda\mathbf{grad}w_n^k dD - \int_{\Gamma_c} w_n^k\lambda h(T_{i+1}-T_\infty)d\Gamma. \tag{17}$$

Assuming that the temperature at the initial time is uniform in the composite material and assuming $\Delta T = T_k - T_\infty$, the equation becomes:

$$\int_{D_c} w_n^k\rho C_p\frac{\Delta T_{i+1}}{\delta T}dD + \int_{D_c}\mathbf{grad}\Delta T_{i+1}\lambda\mathbf{grad}w_n^k dD = \int_{\Gamma_c} w_n^k h\Delta T_{i+1}d\Gamma \tag{18}$$

The matrix system resulting from the spatial discretisation of temperature on the space of nodal elements, by replacing ΔT by its approximation $\Delta T = \sum_{j=1}^{N_n} w_n^j\Delta T_{n,j}$, is as follows:

$$\left(\mathbf{M}_{nn}^{[\rho C_p]} + G^T\mathbf{M}_{aa}^{[\lambda]}G + \mathbf{M}_{nn}^{[h]}\right)\Delta T_{n,i+1} = \mathbf{M}_n^{[P]} + \mathbf{M}_{nn}^{[\rho C_p]}\Delta T_{n,i}, \tag{19}$$

where :

- $\mathbf{M}_{nn}^{[\rho C_p]}$: a mass matrix of dimension $N_n\times N_n$, whose coefficients are given by:

$$m_{nn}^{[\rho C_p]}(i,j) = \int_{D_c}\frac{\rho C_p}{\delta T}w_n^i\cdot w_n^j dD, \tag{20}$$

- $\mathbf{M}_{aa}^{[\lambda]}$: a mass matrix of dimension $N_a\times N_a$, with coefficients:

$$m_{aa}^{[\lambda]}(i,j) = \int_{D_c}\lambda\mathbf{w_a^i}\cdot\mathbf{w_a^j}dD, \tag{21}$$

- $\mathbf{M}_{nn}^{[h]}$: a mass matrix of dimension $N_n\times N_n$, whose coefficients are defined by:

$$m_{nn}^{[h]}(i,j) = \int_{\Gamma_c} hw_n^i\cdot w_n^j d\Gamma. \tag{22}$$

- $\mathbf{M}_n^{[P]}$: a mass matrix of dimension $N_n\times 1$.

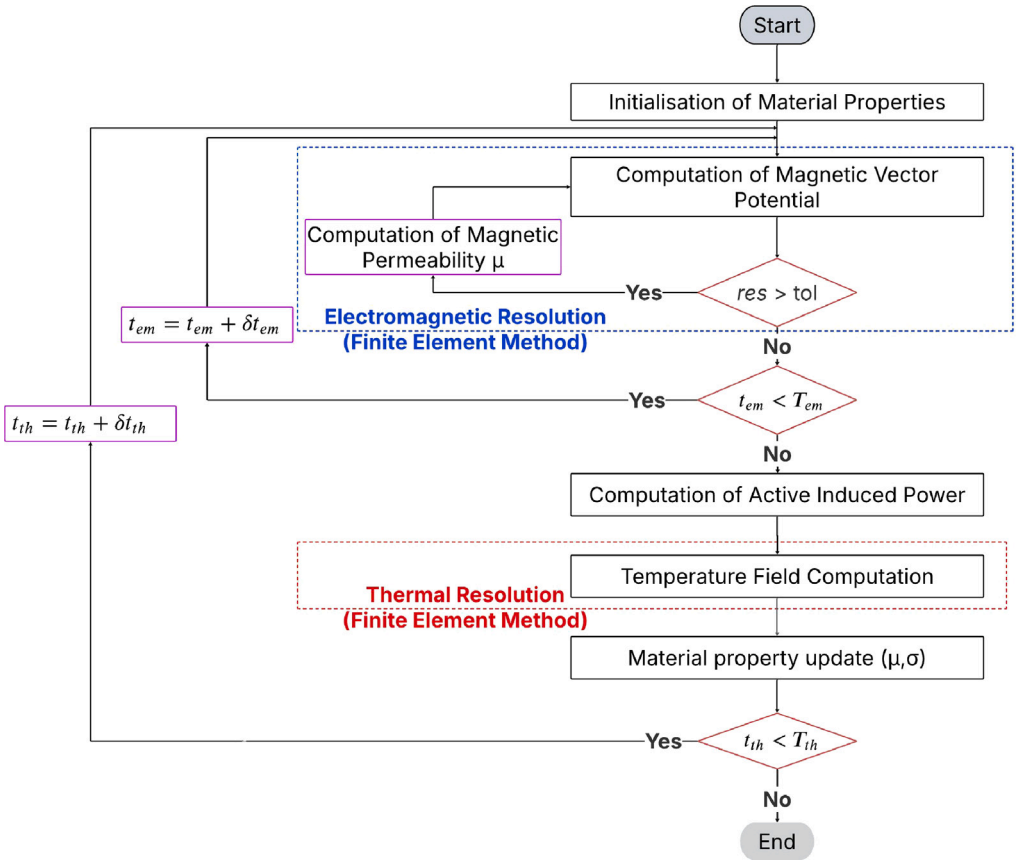

Fig. 10. Weak magnetothermal coupling algorithm.

3.5. Magnetothermal coupling

A weak coupling for magnetothermal modelling, with iterative updating of material properties (magnetic permeability and electrical conductivity) as a function of temperature, is realised for several reasons. Firstly, it maintains a clear separation between the resolution of electromagnetic and thermal problems, while integrating the nonlinear effects induced by temperature. Secondly, it offers better management of computing resources by limiting the number of unnecessary temperature and magnetic field calculations that would be necessary in a strong coupling with a very fine time step. Finally, the iterative updating of properties as a function of temperature compensates in part for the limitations of weak coupling by ensuring progressive convergence towards a stable thermomagnetic state.

Beyond the temperature dependence of material properties, the ferromagnetic nature of Phytherm260® introduces an additional complexity due to the strong nonlinearity of its magnetic behaviour, particularly near the Curie point. To accurately capture this nonlinearity within the electromagnetic resolution step, a Newton–Raphson method to iteratively solve the nonlinear system resulting from the finite element discretisation of Maxwell's equations is used.

At each electromagnetic iteration, the nonlinear relationship between the magnetic field H and the magnetic flux density B necessitates solving a system of equations where the permeability μ varies as a function of the local magnetic field and temperature. The Newton–Raphson method is applied to linearise the system by iteratively updating the magnetic vector potential $\mathbf{A}$ until the convergence criterion is met. This ensures that, at each electromagnetic step, the computed values of $\mathbf{A}$ correctly reflect the nonlinear magnetic response of the material.

To manage the coupling process, two key timescales are introduced implicitly in the algorithm: the electromagnetic resolution time, T_{em}, and the thermal resolution time, T_{th}. The electromagnetic model is iteratively solved as long as the electromagnetic resolution time remains within T_{em}, ensuring that the magnetic field and eddy currents are accurately captured within the given time window. The application of the Newton–Raphson method within each electromagnetic step guarantees convergence towards a physically consistent solution despite the highly nonlinear magnetic behaviour. Similarly, the thermal model is resolved iteratively until the thermal time, T_{th}, reaches the total heating time of the system. This strategy enables the decoupling of the electromagnetic and thermal domains while respecting their inherent timescales, avoiding over-resolution where unnecessary.

Thus, the combined use of weak coupling and Newton–Raphson linearisation effectively addresses the double nonlinearity inherent in the problem: the temperature-dependent variation of electromagnetic properties and the strong magnetic nonlinearity near the Curie temperature. This methodological choice allows for the modelling of the magnetothermal behaviour of Phytherm260® while maintaining computational efficiency over extended simulation periods.

Fig. 10 presents the algorithm used to ensure the weak magnetothermal coupling.

4. Simulation parameters

The geometric and general parameters used for the simulation are listed in Table 3, while the electromagnetic and thermal properties are presented in Tables 4 and 5 respectively. These values have been chosen to be consistent with available experimental data and material specifications.

Electromagnetic properties take into account the dependence of magnetic permeability μ on magnetic field H and temperature T. Electrical conductivity σ also varies with temperature, where an almost linear decrease in this property is observed with increasing temperature.

Table 3
General model parameters.

Parameter	Value
Plate thickness	5 mm
Maximum current	1500 A
Current density	8.33×10^6 A m^{-1}
Coil frequency	20 kHz
Curie point T_C	280 °C

Table 4
Electromagnetic model parameters.

Parameters	Value
Magnetic permeability	$\mu(H,T)$
Electrical conductivity	$\sigma(T)$
Electromagnetic time	$2T = 2/f = 0.1$ ms
Time step	1 µs
Number of time steps	100

Table 5
Thermal model parameters.

Parameter	Value
Density ρ	8200 kgm^{-3}
Thermal conductivity λ	13W m^{-1} K^{-1}
Specific heat capacity C_p	500 J Kg^{-1} K^{-1}
Heating time	200 s
Time step	1 s
Number of time steps	200

These variations are essential for capturing the nonlinear behaviour of materials subjected to an oscillating electromagnetic field.

The thermal conductivity λ, density ρ, and specific heat C_p are considered constant to simplify the model, although the temperature dependence of the electrical conductivity is taken into account. These data are used to capture the heat transfer associated with induction heating.

It is crucial to define an appropriate time duration for the electromagnetic analysis. The electromagnetic time, denoted as T_{em}, corresponds to the period of variation of the simulated magneto-harmonic phenomenon. To ensure accurate results while minimising computational costs, it is necessary to determine the minimal duration required to achieve a stable response of physical quantities, particularly the total induced power.

A simulation was performed over a duration equivalent to ten electromagnetic periods ($t_{\text{em}} = 10T$). Fig. 11 illustrates the evolution of the total induced power as a function of electromagnetic time at an ambient temperature of 20 °C.

From the second period onwards, the variations in P_{ind} become periodic and stabilised, indicating the end of the initial transient regime. The near-identical repetition of cycles after $t = 2T$ reflects convergence towards a steady-state regime. This implies that beyond this duration, the temporal variations of the induced power no longer provide significant additional information that could influence the physical results or conclusions. The electromagnetic time is then fixed at two periods and each period contains 50 iterations.

Table 6 summarises the values of the total induced power in the plate for each electromagnetic period. These values were obtained through magneto-harmonic modelling. It is observed that the power gradually increases during the initial periods, reflecting transient behaviour. From the second period onward, the computed values stabilise, converging to a constant value of 23.66 W. This confirms that two electromagnetic periods are sufficient to capture the established behaviour of the system.

This table highlights the convergence of the total induced power towards a constant value after the second period. Therefore, selecting an electromagnetic duration of $t_{\text{em}} = 2T$ appears to be a judicious choice, ensuring accurate modelling of the studied phenomena while optimising computational resources. Extending the simulation beyond this duration would yield no significant benefit in terms of accuracy or additional information, thus confirming the efficiency and relevance of this approach.

Table 6
Evolution of the total induced power P_{ind} in the plate as a function of the electromagnetic period. The results were obtained using magneto-harmonic modelling at 2020 °C.

Period	1	2	3	4	5	6	7	9	10
Total induced power (W)	19.64	23.65	23.68	23.69	23.66	23.66	23.66	23.66	23.66

In conclusion, the analysis of the induced power evolution and the observed convergence validate the choice of a temporal duration of $2T$ as representative of the steady-state regime.

5. Numerical results

5.1. Induced power evolution

The evolution of the induced active power within the simulated ferromagnetic plate, calculated from the magnetic vector potential **A** has been analysed. The induced active power density is obtained by integrating the induced power density on each element of the digital mesh, which is calculated from the currents induced in the plate. This integration is performed over the second period of electromagnetic time set at $2T = 0.1$ ms, to capture a stable regime of electromagnetic oscillations. Then, to obtain the total active power induced at each thermal instant, the active power density is multiplied by the area of the corresponding element, before being aggregated over all the elements of the plate. This methodology allows us to follow, in the form of a time vector, the evolution of the induced active power throughout the heating process. Fig. 12 shows the temporal evolution of the active power induced within the plate during the thermal simulation. The x-axis corresponds to the heating time in seconds, while the y-axis represents the induced active power. The curve shows a marked decrease in active power, followed by a stabilisation phase at around 1 kW.

At the start of the heating process, the induced active power is relatively high, reaching an initial value of around 10 kW. However, this power decreases rapidly to reach a stabilised value of around 1 kW after about 66 s. This decrease is directly linked to changes in the magnetic properties of the material, in particular the dependence of the magnetic permeability μ on temperature and magnetic field. As the temperature increases and approaches the Curie point $T_C = 280$ °C, the magnetic permeability drops significantly due to the transition of the material from the ferromagnetic state to the paramagnetic state. This transition leads to a reduction in the electromagnetic induction effect, and therefore a reduction in the induced current density. As a result, the active power generated by these currents decreases concomitantly. Once the Curie temperature is reached, the magnetic permeability becomes almost constant and the material loses its ferromagnetic properties, which explains why the active power stabilises at around 1 kW.

Between 50 s and 75 s, the power curve shows slight but visible oscillations. These oscillations are mainly due to transient effects associated with the thermal and magnetic dynamics near the Curie temperature. In this temperature range, the magnetic permeability still varies nonlinearly, creating fluctuations in the induced current density and, consequently, in the power density. Local variations in temperature gradients within the plate can also contribute to these oscillations, by locally modifying electrical conductivity and power dissipation.

The final stabilisation of active power can also be interpreted as a manifestation of the material's thermal self-regulation. Once the Curie temperature is reached, the disappearance of the ferromagnetic properties prevents any further increase in induced currents, thus limiting power dissipation to relatively low levels. This self-regulating property

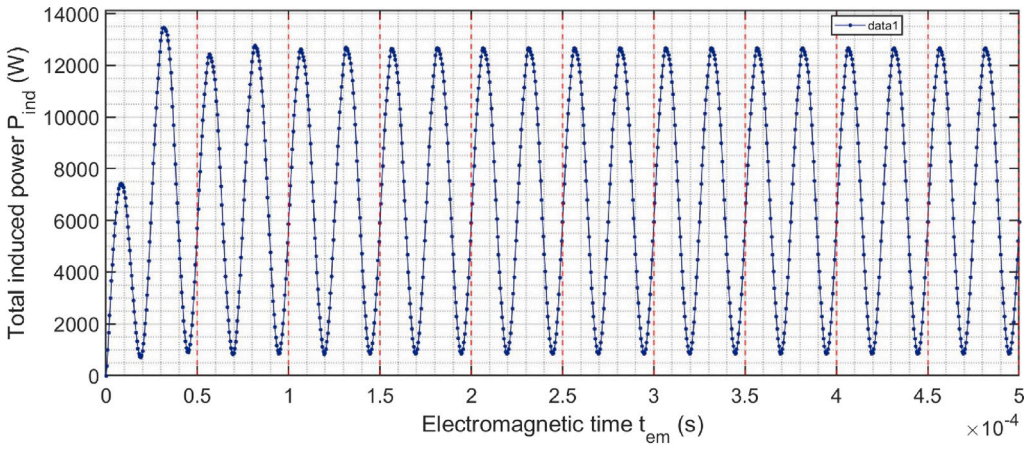

Fig. 11. Evolution of the total induced power P_{ind} as a function of the electromagnetic time ($T_{\text{em}} = 10T$) at a temperature of 20 °C.

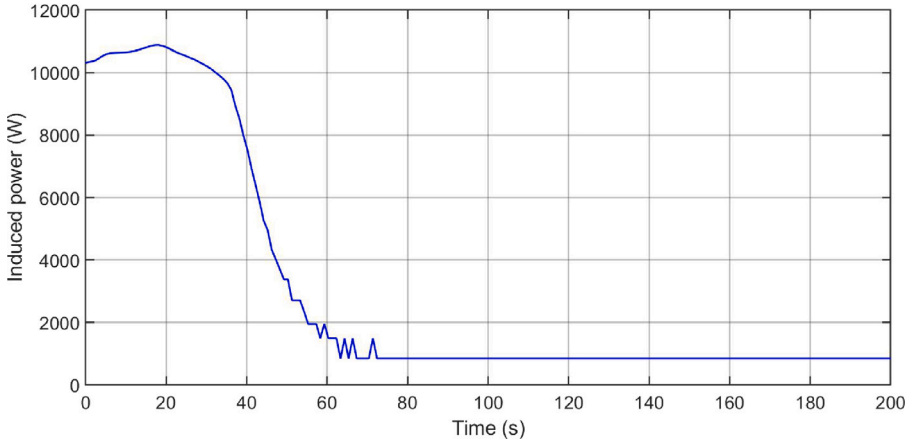

Fig. 12. Induced active power as a function of heating time.

is intrinsic to ferromagnetic materials and is an advantage for applications where precise temperature control is required. Thus, the temporal evolution of the induced active power directly reflects changes in the magnetic and thermal properties of the material, in particular the ferromagnetic–paramagnetic transition [29]. This analysis highlights the importance of taking into account the temperature dependence of magnetic permeability in numerical simulations and demonstrates the ability of the model developed to capture these complex phenomena.

5.2. Temperature evolution

In this subsection, we analyse the temporal evolution of the temperature within the simulated ferromagnetic plate. This result is obtained by solving the heat equation using the finite element method. Fig. 13 shows the evolution of temperature as a function of heating time. The x-axis corresponds to the time expressed in seconds, while the y-axis represents the temperature in degrees Celsius.

The curve shows a gradual and regular rise in temperature, from the ambient temperature of 20 °C to the Curie temperature of 280 °C. This rise phase is characterised by a transient regime dominated by the dissipation of active power induced within the material, generated by induced currents and converted into heat. This temperature rise takes place over about 66 s, after which the curve shows almost perfect stabilisation around the Curie temperature until the end of the heating time heatThermal2020.

The observed evolution highlights a key phenomenon: the thermal self-regulation of the material. This particular behaviour can be explained by the intrinsic properties of the ferromagnetic material. Below the Curie temperature, the material retains its ferromagnetic properties, resulting in high magnetic permeability and significant generation of induced currents. However, as the temperature increases and approaches the Curie temperature, the magnetic permeability decreases in a nonlinear fashion, due to the gradual transition of the material to the paramagnetic state. This change reduces induced currents and, consequently, heat dissipation, which slows the temperature rise and leads to thermal stabilisation around 280 °C.

This thermal self-regulation is the direct result of the complex interaction between electromagnetic and thermal phenomena in the material. On reaching the Curie temperature, the loss of ferromagnetic properties limits heat generation, while thermal diffusion, which tends to balance temperature gradients, becomes the dominant mechanism [30]. This phenomenon is of particular interest in applications where precise temperature control is required, such as induction heating or localised heat treatment. It also illustrates the importance of the material's magnetic properties in the dynamics of heat transfer.

The thermal stabilisation observed around the Curie temperature is a central feature of this work, as it confirms the ability of the model developed to capture self-regulation phenomena [31]. This behaviour, which is often sought after in industrial applications, makes it possible to guarantee the thermal safety inherent in the process, by preventing any uncontrolled temperature rise.

This curve illustrates not only the validity of the proposed thermal and electromagnetic model but also the relevance of combining these two disciplines to explain complex phenomena such as thermal self-regulation. These results highlight the fundamental role of the ferromagnetic–paramagnetic transition in the thermal dynamics of the

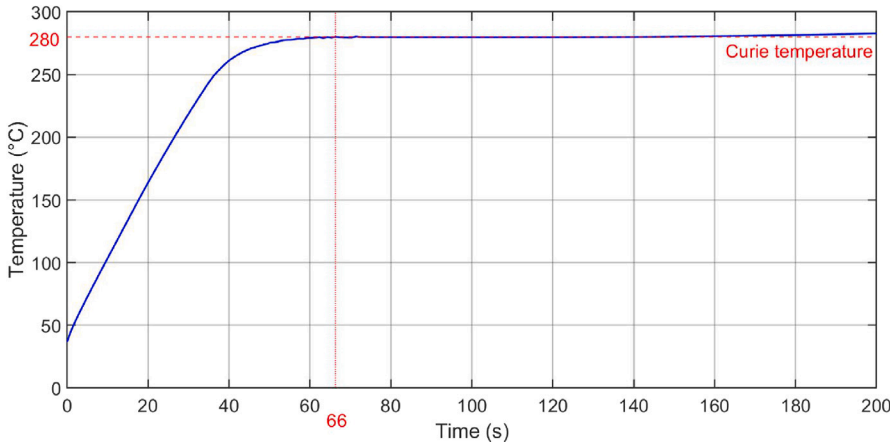

Fig. 13. Temperature as a function of heating time. The red line indicates the Curie temperature (T_C = 280 °C).

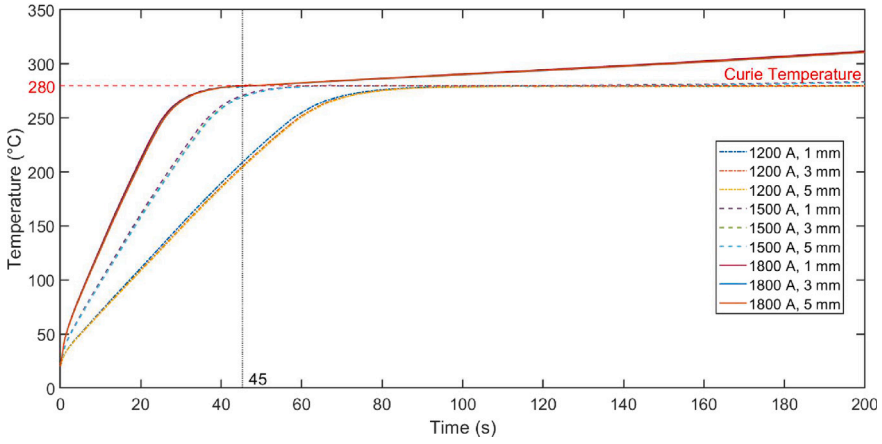

Fig. 14. Influence of the electric current and plate thickness on the temperature evolution.

material and pave the way for future investigations aimed at optimising this type of behaviour for practical applications.

6. Sensitivity analysis

The fundamental thermal and electromagnetic behaviours of the system were established, highlighting the interplay between induced power, thermal evolution, and material properties near the Curie temperature. Building on these findings, it is crucial to evaluate how external factors, such as the applied electric current and the thickness of the ferromagnetic plate, influence the system's thermal response and self-regulation behaviour. To this end, a sensitivity analysis was conducted, providing deeper insights into the system's operational boundaries and potential for optimisation.

This sensitivity study aims to evaluate the impact of two key simulation parameters—the imposed electric current and the thickness of the ferromagnetic plate—on the system's thermal behaviour. Specifically, the temperature evolution was simulated for nine different combinations of these parameters: three values of the electric current (I = 1200 A, I = 1500 A, and I = 1800 A) and three plate thicknesses (e = 0.001 m, e = 0.003 m, and e = 0.005 m). Fig. 14 presents the temperature evolution as a function of time for each combination of these parameters.

The resulting curves provide critical insights into how each parameter affects the thermal response and, in particular, the phenomenon of thermal self-regulation, which is a central focus of this study. This phenomenon is intrinsically linked to the ability of ferromagnetic materials to lose their magnetism above the Curie temperature. A detailed analysis of the results reveals several significant trends.

First, the influence of the electric current is particularly pronounced. When the electric current reaches a high value I = 1800 A (represented by the solid lines), the temperature exceeds the Curie temperature without stabilisation. Contrary to expectations, thermal regulation does not occur in this case: the temperature continues to rise, although with a slightly reduced slope after surpassing the Curie temperature. This behaviour can be attributed to insufficient dissipation of accumulated thermal energy, exacerbated by the high current intensity, which generates increased Joule heating losses. As a result, thermal self-regulation becomes ineffective at this level of current.

At an intermediate current of I = 1500 A (dashed lines), the phenomenon of thermal self-regulation is observed. The curves show that the temperature approaches the Curie temperature and exhibits characteristic oscillations around this value. These oscillations reflect periodic transitions between the ferromagnetic and paramagnetic states of the material: the appearance and disappearance of ferromagnetic properties directly influence the magnetic permeability and, consequently, the induced power in the system. These results align with theoretical expectations for Curie-point materials, where self-regulation is achieved through the interaction of electromagnetic and thermal properties.

For a lower current (I = 1200 A, dotted lines), thermal self-regulation is also observed, but the attainment of the Curie temperature occurs more gradually. This can be explained by a more moderate generation of Joule heating, which delays the temperature rise. However, once the Curie temperature is reached, thermal oscillations also appear, demonstrating behaviour similar to that observed at I = 1500 A, albeit with slower temporal dynamics.

Regarding the thickness of the ferromagnetic plate, its influence is less pronounced but remains noticeable. At a constant current, the temperature rise is slightly faster for thinner plates ($e = 1\,\text{mm}$) compared to thicker ones ($e = 5\,\text{mm}$). This difference can be attributed to the dependence of Joule heating losses on the system's geometry. A thinner plate is associated with lower thermal inertia, allowing a more rapid temperature increase. However, this trend does not significantly affect the general self-regulation behaviour: for all three thicknesses, the curves reach the Curie temperature at different times but exhibit similar behaviours once this temperature is achieved.

Finally, it is important to emphasise that thermal self-regulation relies on a delicate balance between the system's electrical parameters and thermal properties. Excessively high current intensity, as observed for $I = 1800\,\text{A}$, can disrupt this balance and compromise stabilisation around the Curie temperature. Conversely, moderate current intensities ($I = 1200\,\text{A}$ or $I = 1500\,\text{A}$) effectively exploit this intrinsic property of ferromagnetic materials, rendering the system thermally stable and better suited for applications where thermal regulation is critical.

These findings highlight the importance of selecting appropriate simulation parameters, not only to ensure a rapid temperature rise but also to guarantee precise thermal control. They also provide valuable insights for optimising operating conditions in practical applications involving Curie-point materials.

7. Computation time analysis and algorithmic bottlenecks

An analysis of the simulation times enables us to assess the distribution of computational costs between the different stages of the calculation. The complete simulation required a total time of 2 h 16 min 8 s. A detailed study of the average times per thermal, electromagnetic, and nonlinear iteration provides a better understanding of the time structure of the calculation.

On average, a magnetothermal iteration takes 40.8 s, which represents the main component of the computational cost. This value includes the cumulative time of the electromagnetic iterations and the finite element solution of the heat equation. For each magnetothermal iteration, the solver performs 100 electromagnetic iterations, each taking an average of 0.4 s. The contribution of the electromagnetic iterations to a magnetothermal iteration can therefore be estimated by multiplying 100 by 0.4 s, giving a total of 40 s. By isolating this contribution from the average time of a thermal iteration, we obtain the clean time for solving the heat equation:

$$T_{\text{th}} = T_{\text{magth}} - 100 \times T_{\text{em}} = 40.788 - 40.57 = 0.218\ \text{s} \tag{23}$$

The electromagnetic iteration is the most intensive phase of the simulation. The choice of a Newton–Raphson algorithm to take account of magnetic nonlinearity also leads to internal sub-iterations, the average time per iteration of which is estimated at 4 ms. Given that each electromagnetic iteration requires several resolutions of linear systems depending on the number of nonlinear iterations, this relatively low time suggests rapid convergence of the Newton–Raphson method within the framework of the model studied.

The time distribution within a magnetothermal iteration highlights the predominance of the electromagnetic calculation, which represents around 99.5% of the time of a magnetothermal iteration, compared with only 0.5% for the thermal resolution itself. This observation confirms that most of the computational effort is devoted to simulating the magnetic field, while the heat equation is solved relatively quickly in comparison.

8. Conclusion

A two-dimensional multiphysics and multiscale model to accurately model the behaviour of Curie point materials heated by electromagnetic induction was developed. This work required a rigorous and progressive approach to overcome the numerical and physical challenges inherent in this type of problem.

A fundamental step in this development was the implementation of a mesh adapted to the specific characteristics of the problem studied. Using the GMSH software, we designed a rectangular mesh that proved particularly effective in managing the numerical problems associated with the significant variations in magnetic permeability as a function of temperature. These variations, which are directly linked to the ferromagnetic behaviour of the material, induce very pronounced gradients in the electromagnetic and thermal fields, requiring fine, localised resolution. Unlike a conventional triangular mesh, the rectangular mesh enabled us to significantly reduce numerical errors, by ensuring better quality and regularity of the elements, while respecting the geometric constraints imposed by the thickness of the skin and the zones of high magnetic nonlinearity.

Robust numerical methods were used to deal with the nonlinear aspects of the system, particularly those arising from the dependence of magnetic permeability on temperature and magnetic field. In particular, the Newton–Raphson method was used to linearise and solve the coupled equations governing the electromagnetic and thermal phenomena. This approach stabilised the calculations while ensuring rapid and accurate convergence, even under conditions of significant nonlinearity.

Once the model had been implemented, simulations were carried out to analyse the evolution of the physical quantities characteristic of the system. We studied in detail the power induced in the plate and its influence on the temporal evolution of the temperature, taking into account the two-dimensional dependence of the problem. The results revealed the existence of a remarkable phenomenon of thermal self-regulation under specific conditions. This phenomenon, linked to the appearance and disappearance of the ferromagnetic property as a function of temperature, enables the system to maintain a stable temperature without the need for sensors or external control. These properties offer promising prospects for industrial induction heating applications, particularly in constrained environments where the simplicity and robustness of the systems are paramount. To gain a better understanding of the conditions under which this self-regulation phenomenon occurs, a sensitivity study was carried out. This study assessed the influence of various parameters on the simulation results, in particular those relating to the thermal and magnetic properties of the materials and the operating conditions. These analyses provided valuable information on the optimal ranges of parameter values required to achieve effective thermal self-regulation. The absence of sensors, coupled with the ability of the material to adapt its thermal response according to its intrinsic properties, gives the system a particularly interesting functional autonomy.

In conclusion, this work has enabled us to develop an accurate dimensioning tool that is suitable for modelling induction heating systems that exploit the ferromagnetic behaviour of Curie point materials. This tool offers considerable flexibility, enabling different configurations and hypotheses to be tested, while guaranteeing accurate modelling of the complex physical phenomena involved. The proposed approach thus paves the way for rational, optimised design of self-regulating heating systems, exploiting the thermomagnetic properties of the materials being heated to achieve passive, reliable and efficient thermal control. Experimental validation is required to confirm the results obtained under the conditions imposed. This phase is essential to ensure the accuracy of the interpretations of thermal self-regulation due to induction heating of ferromagnetic materials, to use this model to predict their behaviour near the Curie point and to integrate them into industrial processes.

CRediT authorship contribution statement

Hakim Oueslati: Writing – review & editing, Writing – original draft, Visualization, Validation, Software, Methodology, Investigation, Formal analysis, Data curation, Conceptualization. **Guillaume Wasselynck:** Writing – review & editing, Visualization, Supervision, Methodology, Formal analysis, Data curation, Conceptualization. **Didier Trichet:** Writing – review & editing, Visualization, Methodology, Formal analysis, Conceptualization. **Simon Morville:** Writing – review & editing, Supervision.

Declaration of competing interest

The authors declare the following financial interests/personal relationships which may be considered as potential competing interests: Hakim Oueslati reports financial support was provided by Jules Verne Institute of Technology. If there are other authors, they declare that they have no known competing financial interests or personal relationships that could have appeared to influence the work reported in this paper.

Acknowledgements

This work is part of the PERFORM project managed by IRT Jules Verne (French Institute in Research and Technology in Advanced Manufacturing Technologies for Composite, Metallic, and Hybrid Structures). The authors would like to express their gratitude to APERAM and Thierry Waeckerle for providing the magnetic data of the Phytherm260® material, specifically designed by APERAM, as well as for supplying material samples and supporting this research.

Data availability

The data that has been used is confidential.

References

[1] T. Waeckerle, Low nickel content fcc alloys: Recent evolution and applications, IEEE Trans. Magn. 46 (2010) 326–332, http://dx.doi.org/10.1109/TMAG.2010.2040465.

[2] T. Waeckerle, H. Fraissé, B. Boulogne, S.L. Spire, New alloys and multilayer configuration of them to get self-regulated temperature cookware (srtc) in induction heating, J. Magn. Magn. Mater. 304 (2006) e844–e846, http://dx.doi.org/10.1016/j.jmmm.2006.03.013, proceedings of the 17th International Symposium on Soft Magnetic Materials.

[3] P. Chevenard, Rev. Métall. 25 (1928).

[4] A. Ahmad, H. Akbar, I. Zada, F. Anjum, A.M. Afzal, S. Javed, M. Muneeb, A. Ali, J.R. Choi, Improvement of the self-controlled hyperthermia applications by varying gadolinium doping in lanthanum strontium manganite nanoparticles, Molecules 28 (2023) http://dx.doi.org/10.3390/molecules28237860.

[5] C. Mazón, L. Quintero Hernández, E. Mazón Valadez, A. Hernández-Sámano, J. Ávila Paz, M. Cano, Developing a self-regulating soldering iron based on induction heating, Dyna (Medellin, Colombia) 83 (2016) 159–167, http://dx.doi.org/10.15446/dyna.v83n196.51208.

[6] Y. Wang, B. Das, T.D. Thorn, S. Huo, J. Evans, M. Newton, Y. Liu, S.G. Advani, D.G. Papageorgiou, E. Bilotti, H. Zhang, Towards highly homogeneous self-regulating heating of smart nanocomposites, Appl. Mater. Today 39 (2024) 102292, http://dx.doi.org/10.1016/j.apmt.2024.102292.

[7] T. Todaka, T. Kishino, M. Enokizono, Low curie temperature material for induction heating self-temperature controlling system, J. Magn. Magn. Mater. 320 (2008) e702–e707, http://dx.doi.org/10.1016/j.jmmm.2008.04.146, proceedings of the 18th International Symposium on Soft Magnetic Materials.

[8] Z. Oudni, H. Mohellebi, M. Féliachi, Effect of Aluminum Layer on Induction Heating Control Case Study Using Finite Elements Method, J. Electr. Syst. (2009) 62–66.

[9] R.S. Ruffini, R.T. Ruffini, V.S. Nemkov, R.C. Goldstein, Computer simulation of induction heating and quenching processes, Flux Mag. (2001).

[10] B. Kane, G. Wasselynck, B.H. Kien, D. Trichet, Focalization of electromagnetic power at the interface between two composites materials for induction welding, Eur. Phys. J. Appl. Phys. (2020).

[11] H. Oueslati, D. Trichet, G. Wasselynck, S. Morville, Modélisation multiphysique des matériaux à bas point de Curie magnétique, in: Symposium Du GÉnie Electrique, L2ep, Lille, France, 2023, URL https://hal.science/hal-04526792.

[12] T. Waeckerle, Étude magnétothermique d'un alliage à bas point de curie en cuisson par induction, in: Symposium de Génie Electrique, Grenoble, France, 2016, URL https://hal.science/hal-01361624.

[13] O. Messal, Caractérisation et ModÉlisation du Comportement ThermomagnÉtique D'Alliages Feni Pour le Prototypage Virtuel (Ph.D. thesis), Université de Lyon, 2013, URL https://theses.hal.science/tel-01130120/.

[14] Thierry Waeckerle, APERAM, Données expérimentales sur XYZ, Données internes, Fichier excel fourni par APERAM dans le cadre du programme PERFORM, 2021, Non publié.

[15] C. Kittel, Introduction to Solid State Physics, eighth ed., Wiley, 2005, URL https://books.google.com/books?hl=en&id=nNpVEAAAQBAJ.

[16] P. Langevin, On the theory of magnetism, Ann. Chim. Phys. 8 (1905) 70–127, http://dx.doi.org/10.1103/PhysRevB.58.14937, URL https://journals.aps.org/prb/abstract/10.1103/PhysRevB.58.14937.

[17] A.T. Bui, Caractérisation et Modélisation du Comportement des Matériaux Magnétiques Doux Sous Contrainte Thermique (Doctoral thesis), Université Claude Bernard - Lyon I, 2011.

[18] D. Jiles, J. Thoelke, M. Devine, Numerical determination of hysteresis parameters for the modeling of magnetic properties using the theory of ferromagnetic hysteresis, IEEE Trans. Magn. 28 (1992) 27–35, http://dx.doi.org/10.1109/20.119813, URL https://ieeexplore.ieee.org/document/119813.

[19] M. Fisk, M. Ristinmaa, A. Hultkrantz, L.-E. Lindgren, Coupled electromagnetic-thermal solution strategy for induction heating of ferromagnetic materials, Appl. Math. Model. 111 (2022) 818–835, http://dx.doi.org/10.1016/j.apm.2022.07.009, URL https://www.sciencedirect.com/science/article/pii/S0307904X22003298.

[20] J. Zhao, T. Yang, Finite element mesh optimization for ferromagnetic materials in electromagnetic simulations, IEEE Trans. Magn. 57 (2021) 1–10, http://dx.doi.org/10.1109/TMAG.2021.3046234, URL https://ieeexplore.ieee.org/document/9285864.

[21] E. Jones, K. Murray, Finite element modeling of heat distribution in ferromagnetic materials, J. Therm. Anal. 110 (2015) 221–238, http://dx.doi.org/10.1007/s10973-015-4576-2, URL https://link.springer.com/article/10.1007/s10973-015-4576-2.

[22] A. Smith, K. Nielsen, D. Christensen, C. Bahl, R. Bjørk, J. Hattel, The demagnetizing field of a nonuniform rectangular prism, J. Appl. Phys. 107 (2010) 103910.

[23] C. Monzel, G. Henneberger, Temperature solver for highly nonlinear ferromagnetic materials for thin moving sheets in transversal flux induction heating, IEEE Trans. Magn. 38 (2002) 937–940.

[24] C. Geuzaine, J.-F. Remacle, Gmsh: A 3-d finite element mesh generator with built-in pre- and post-processing facilities, Internat. J. Numer. Methods Engrg. 79 (2009) 1309–1331.

[25] C. Courtès, M. Boileau, R. Côte, P.-A. Hervieux, G. Manfredi, Micromagnetic simulations of the size dependence of the curie temperature in ferromagnetic nanowires and nanolayers, J. Magn. Magn. Mater. 598 (2024) 172040.

[26] M. Ndiaye, Outils de Modélisation et Règles de Conception Globale de Procédés D'assemblage de Composites Thermoplastiques par Induction Électromagnétique (These de doctorat), Nantes Université, 2022.

[27] P. Ferrouillat, Développement de Formulations Éléments Finis 3D en Potentiel Vecteur Magnétique : Application aux Machines Asynchrones en Mouvement (These de doctorat), Université Grenoble Alpes (ComUE), 2015.

[28] H.S. Carslaw, J.C. Jaeger, Conduction of Heat in Solids, second ed., Oxford University Press, Oxford, 1986.

[29] R.M. Bozorth, Ferromagnetism and its applications, Phys. Rev. 80 (1951) 508–516, http://dx.doi.org/10.1103/PhysRev.80.508, URL https://journals.aps.org/prb/abstract/10.1103/PhysRev.80.508.

[30] P. Garcia, A. Ruiz, Correlation of magnetic and thermal properties in alloys, Mater. Des. 141 (2018) 302–317.

[31] B. Peterson, R. King, Experimental validation of electromagnetic heating models for ferromagnetic materials, J. Comput. Phys. 270 (2014) 355–369.